Onset of anharmonicity and thermal conductivity in SnSe

Michael Y. Hu, Xue Yong, Niall J. English, and John S. Tse

Phys. Rev. B **104**, 184303 — Published 18 November 2021

DOI: 10.1103/PhysRevB.104.184303

Onset of anharmonicity and thermal conductivity in SnSe

Michael Y. Hu,[1,*] Xue Yong,[2] Niall J. English,[3] and John S. Tse[2,†]

[1] *Advanced Photon Source, Argonne National Laboratory, Argonne, IL 60439*
[2] *Department of Physics and Engineering Physics, University of Saskatchewan, Saskatoon S7N 5E2, Canada*
[3] *School of Chemical and Bioprocess Engineering, University College Dublin, Ireland*

(Dated: October 10, 2021)

The anharmonicity in SnSe is investigated through the analysis of moments of ^{119}Sn Nuclear Resonant Inelastic X-ray Scattering and *ab initio* Molecular Dynamics calculations. Experimental evidences show that the anharmonic behaviour started around 300 K, substantially lowered than the usually suggested structural transition at 800 K. Both theory and experiments reveal substantial lifetime broadening and frequency renormalization of the optical phonons. Thermal conductivities calculated from the temporal energy moment using Einstein diffusion equation are in good agreement with previous experiments. The abrupt increase of the thermal power near the 800 K is driven by an electronic factor and not by the enhanced anharmonicity due to structural change.

Pure crystalline tin-selenium (SnSe) is a small band gap (0.86 eV) semiconductor [1] with a fairly high electrical resistivity of 20 Ω cm at room temperature [2]. It has been reported that SnSe has a very low thermal conductivity and a high thermal power [3]. The remarkable properties make it a potential high efficiency thermoelectric material converting heat into electrical power. Since then, the electronic structure and thermal transport mechanism have been studied extensively employing a variety of experimental and theoretical techniques [4]. The ambient crystal structure of SnSe is orthorhombic $Pnma$, formed from stacking of corrugated SnSe layers along the crystallographic a-axis [5–7]. Thus, thermal transport is expected to be inhibited along that direction. Near 800 K, the crystal transforms into an entropically stable orthorhombic $Cmcm$ structure, which leads to changes in the immediate bonding environment for Sn.

Most theoretical studies have focussed on the lattice instability at high temperatures close to the structural transition. State-of-the-art lattice dynamics calculations incorporating anharmonic corrections [8] and renormalization of the phonon frequencies [9] support this description and have provided estimates on the thermal conductivity along the three principal crystal axes which are in reasonable accord with experiments. The notion that the intrinsic anharmonicity in SnSe is due to lattice instability enhanced by the structural transformation is inconsistent with the observed thermal conductivity, which is relatively flat at high temperatures and shows no abrupt decrease around the phase transition. It is noteworthy that the structural transformation is also associated with two orders of magnitude increase of electrical conductivity, a drop in Seebeck coefficient, which when combined with the already low thermal conductivity lead to a very high thermoelectric figure of merit (ZT). Lattice anharmonicity of SnSe has been studied with single crystal neutron inelastic scattering to show phonon mode softening and linewidth broadening [10].

We have introduced a direct local probe of the potential experienced by selected atoms in condensed phases using the technique of nuclear resonant inelastic x-ray scattering (NRIXS). Moments of the NRIXS energy spectra provide unique information on local atomic potential [11]. It is revealed that the anharmonic effects in SnSe are already set in around 300 K affecting the low and high energy optical vibrations. This observation is supported by explicit calculations of the Sn partial phonon DOS (Density of States) using *ab initio* Molecular Dynamics (AIMD) [12] and the results of the thermal conductivity computed using a new direct method via the evaluation of the diffusion of the energy moment [13–15].

NRIXS is an X-ray spectroscopy method to study atomic vibrations and dynamics [16], currently done with synchrotron radiation at third generation high energy X-ray facilities. It finds a wide range of applications in condensed matter physics, materials science, chemistry, biophysics, geosciences, and high-pressure research. In an NRIXS experiment, one measures the number of nuclear resonant absorption events as a function of energy transfer from an incident x-ray beam to the sample under study. Besides the resonant enhancement so that minute sample can be studied, a unique aspect of using resonant isotopes is its isotopic and atomic selectivity. This means that vibrations can be probed locally in systems that have resonant isotopes in specific places, *e.g.*, biomolecules, catalysts, thin films, and materials under extremely high pressures. Many atomic dynamics and lattice thermodynamics information can be extracted from NRIXS measurements [11]. Phonon DOS, which characterizes lattice dynamics of a material, can be derived under the quasi-harmonic approximation [17, 18].

In an NRIXS experiment, the count rates observed are proportional to a phonon excitation probability density function $S(E, \boldsymbol{k})$ [19–21], where E is the energy difference between incident X-ray and the nuclear resonance energy, and $\hbar\boldsymbol{k}$ is the incident photon momentum and a constant for all practical purposes here. The measured

* myhu@anl.gov
† John.Tse@usask.ca

spectrum is proportional to the sum of the cross sections from all resonant nuclei, whose number is $\tilde{N}$, which may be smaller than N, the number of all atoms in the sample. $S(E, \boldsymbol{k})$ is a dynamical function related to the particle autocorrelation function,

$$S(E, \boldsymbol{k}) = \frac{1}{2\pi\hbar} \int e^{i(\boldsymbol{k}\boldsymbol{r} - \frac{E}{\hbar}t)} \, G_A(\boldsymbol{r}, t) \, d\boldsymbol{r} \, dt \,, \tag{1}$$

$$G_A(\boldsymbol{r}, t) = \frac{1}{\tilde{N}} \left\langle \sum_{\nu}^{\tilde{N}} \int d\boldsymbol{r}' \delta\Big(\boldsymbol{r} + \boldsymbol{r}_\nu(0) - \boldsymbol{r}'\Big) \, \delta\Big(\boldsymbol{r}' - \boldsymbol{r}_\nu(t)\Big) \right\rangle_T \tag{2}$$

where $\boldsymbol{r}_\nu$ is the position of the ν-th resonant nucleus. The statistical average at a given temperature T is indicated by $\langle \cdots \rangle_T$. It should be emphasized here that Eq. (2) is an auto-correlation function. As a result, $S(E, \boldsymbol{k})$ obtained from NRIXS is a function of energy transfer and incident X-ray momentum, in contrast to the dynamic structure factor, $S(\boldsymbol{q}, \omega)$, a function of energy and momentum transfers. It can be interpreted as the phonon excitation probability density function. In the weak scattering limit, it is a sum over all nuclei the transition matrix elements due to a sudden momentum transfer [22],

$$S(E, \boldsymbol{k}) = \frac{1}{\tilde{N}} \sum_{\nu} \sum_{i,f} g_i \left| \langle f | e^{i\boldsymbol{k}\boldsymbol{r}_\nu} | i \rangle \right|^2 \delta(E + E_i - E_f) \,, \tag{3}$$

where g_i is the statistical distribution of initial lattice state $|i\rangle$ at a finite temperature.

Sum rules of the moments of $S(E, \boldsymbol{k})$ are related to dynamical properties of the resonant nuclei in a sample [11, 22]. Its central moments with respect to the nuclear recoil energy $E_R = (\hbar k)^2/2\tilde{m}$ have more straightforward interpretations and are defined in Ref. [11] as,

$$R_l(\boldsymbol{k}) \equiv \int_{-\infty}^{+\infty} (E - E_R)^l \, S(E, \boldsymbol{k}) \, dE \,. \tag{4}$$

Substituting Eq.(3) in the above definition, we have,

$$R_l(\boldsymbol{k}) = \frac{1}{\tilde{N}} \sum_{\nu} \sum_{i} g_i \left\langle i \left| \left(H - E_i - \frac{\hbar\boldsymbol{k}}{\tilde{m}} \boldsymbol{p}_\nu \right)^l \right| i \right\rangle \,, \tag{5}$$

where lattice Hamiltonian is,

$$H = \sum_{\mu}^{N} \frac{\boldsymbol{p}_\mu^2}{2m_\mu} + V(\boldsymbol{r}_1, \boldsymbol{r}_2, ..., \boldsymbol{r}_N) \tag{6}$$

and V is the many-body lattice potential.

Here we focus on the 3rd moment, as it is related to the atomic potentials experienced by the nuclear resonant isotopes [22],

$$R_3 = \frac{\hbar^2 E_R}{\tilde{m}} \left\langle \frac{\partial^2 V}{\partial z^2} \right\rangle \,, \tag{7}$$

where z is the coordinate along incident photon direction $\hat{\boldsymbol{k}} = \boldsymbol{k}/k$. Taking the expansion of V up to the quartic term [11], we have

$$\frac{\partial^2 V}{\partial z^2} = K_{\hat{\boldsymbol{k}}} + A_{\hat{\boldsymbol{k}}} \delta_{\hat{\boldsymbol{k}}} + \frac{B_{\hat{\boldsymbol{k}}}}{2} \delta_{\hat{\boldsymbol{k}}}^2 \tag{8}$$

with the atomic displacement $\delta_{\hat{\boldsymbol{k}}}$ along $\hat{\boldsymbol{k}}$, directional force constant $K_{\hat{\boldsymbol{k}}} = \frac{\partial^2 V}{\partial z^2}$, and the 3rd- and 4th-order coupling parameters $A_{\hat{\boldsymbol{k}}} = \frac{\partial^3 V}{\partial z^3}$, $B_{\hat{\boldsymbol{k}}} = \frac{\partial^4 V}{\partial z^4}$. They are all evaluated at the equilibrium atomic positions. At equilibrium, the mean displacement in any direction is zero. This leaves two terms on the right hand side of Eq. (7), which now reads,

$$R_3 = \frac{\hbar^2 E_R}{\tilde{m}} \left[K_{\hat{\boldsymbol{k}}} + \frac{B_{\hat{\boldsymbol{k}}}}{2} \langle \delta_{\hat{\boldsymbol{k}}}^2 \rangle \right] \,, \tag{9}$$

where $\langle \delta_{\hat{\boldsymbol{k}}}^2 \rangle$ is the atomic mean square displacement in $\hat{\boldsymbol{k}}$-direction. It can be derived from a NRIXS spectrum as well, through the following relationship with directional Lamb-Mössbauer factor,

$$f(\boldsymbol{k}) = e^{-k^2 \langle \delta_{\hat{\boldsymbol{k}}}^2 \rangle} \tag{10}$$

At different temperatures or pressures, the atomic potentials are different in principle. Thus, one will have different K's and B's in Eq. (9). However, if the variations of the parameters and in the shape of potential are small between two nearby measurements, one can then approximate them to be constants, and solve for the quadratic and quartic terms of the atomic potential experienced by the resonant isotopes.

NRIXS has been applied to single crystal SnSe at room temperature to check for directional phonon DOS both in-plane and along a axis [23]. Here we study powder SnSe at various temperatures to investigate lattice anharmonicity.

Polycrystalline tin selenide (SnSe) was ordered from Sigma-Aldrich (Lot# MKBP1594V, PCode: 1001573597). The product specification declared a purity of 99.995% based on trace metals analysis. This SnSe powder was mixed with GE varnish and attached to the end of a copper post connected to the cold finger of a Displex cryostat. NRIXS measurements were then conducted at temperatures from 160 to 390 K, at the Advanced Photon Source (APS) beamline 30ID. Energy scans covering phonon spectral range and around ^{119}Sn nuclear resonant energy of 23.88 keV were conducted using a tunable high resolution monochromator with an energy bandwidth of 1 meV [24]. Data was processed using both SciPhon [25] and PHOENIX [26].

The results are shown in Fig. 1 for Sn partial phonon DOS. Temperature dependence of f-factor and the third moment R_3, and R_3 *vs.* mean square displacement $\langle \delta_{\hat{\boldsymbol{k}}}^2 \rangle$ are plotted in Fig. 2. Lamb-Mössbauer factors f drop with increasing temperatures, which is expected, however are almost flat at high temperatures. R_3 are flat

to slightly decreasing in the range studied and are substantially higher around 300 K. This indicates that the lattice being harmonic at low temperatures, while exhibiting highly anharmonic behaviour at around 300 K. Two regions stand out above the almost flat force constants in Fig. 2(b). One at around $\langle \delta^2_{\hat{k}} \rangle = 0.012$, with corresponding temperatures from 255 to 298 K, where the quartic term of the potential (slope of the points) is positive. The other for $\langle \delta^2_{\hat{k}} \rangle > 0.014$, with 340 to 390 K, where the slope is sharply negative. Both cases indicate highly anharmonic potentials, while a negative quartic term might cause lattice instability.

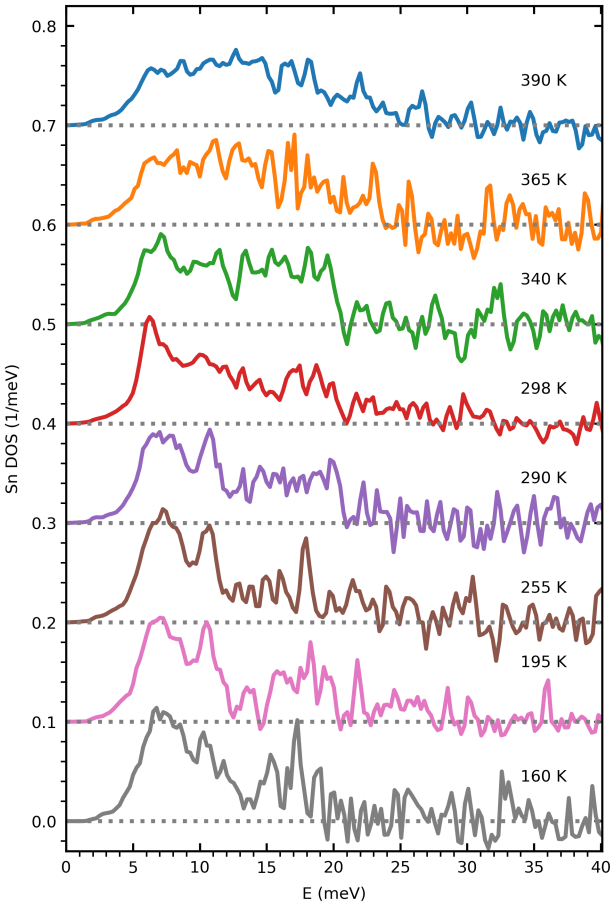

FIG. 1. Sn partial phonon DOS derived from NRIXS measurements. DOS are normalized to 1.

As seen in Fig. 2(a) the Lamb-Mössbauer factors f drop with increasing temperatures. This fact makes it difficult for reliable data reduction at high temperatures, due to dominating multi-phonon contributions in the measured spectra. Thus going above 400 K is very challenging.

AIMD calculations were performed at selected temperatures between 200 and 800 K using the VASP code with ultrasoft pseudopotentials [27, 28] for the Sn and Se atoms with a plane wave energy cutoff of 155 eV. Model cells and the atom positions were sampled at the

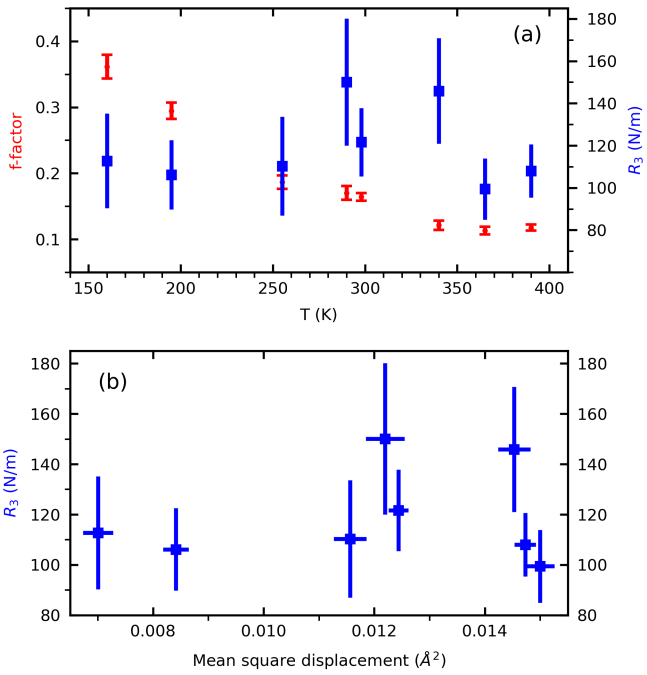

FIG. 2. Temperature dependence of f-factor and the third moment R_3 (a), and R_3 *vs.* $\langle \delta^2_{\hat{k}} \rangle$ (b) as derived from NRIXS measurements. In plot (a), f-factors are represented by small dots with scale on the left axis, while R_3 with squares and scale on the right.

respective temperature using isobaric-isothermal ensemble (NPT) [29]. Once the average unit cell parameters at each temperature have been determined, canonical ensemble (NVT) MD [29] were performed to examine the equilibrium dynamic and transport properties. Langevin thermostat and barostat were used in NVT and NPT molecular dynamics calculations. NPT and NVT calculations at 200 K were performed with a time step of 1.0 fs. A larger time step of 1.5 fs was used at higher temperatures. At each temperature, the NPT equilibration often achieved after 5000 time steps. The trajectory for an additional 10000 steps were collected and the atomic velocity autocorrelation functions over time were computed from the trajectory. The total and Sn, Se partial vibration density of states were then obtained from the Fourier transform of the velocity correlation functions. Due to slow convergence in the calculation of transport properties, NVT simulation of 60-80 ps were required.

A model system was constructed from a 2x5x5 replication of the unit cell of the *Pnma* unit cell [6, 7] consisting of 200 SnSe units. The average cell parameters were computed from the equilibrated trajectories (Table I). Both the trend and absolute values are in agreement with experimental results [30, 31]. Calculated c and b lattice parameters are very close to those derived from XRD measurements. In particular, the observed differences between c and b axes in *Pnma* phase are correctly predicted. The calculated a parameters are consistently

higher than measured values, from about 1% at 300 K to 7% at 800 K. The spontaneous second-order structure transformation from *Pnma* to *Cmcm* is reproduced by the calculation at 800 K.

TABLE I. Lattice constants computed from AIMD simulations.

T(K)	a (Å)	b (Å)	c (Å)
200	11.330	4.204	4.524
300	11.656	4.184	4.494
410	11.791	4.233	4.505
600	11.745	4.234	4.444
800	12.588	4.331	4.356

The theoretical anisotropic atomic displacement parameters (ADPs) for Sn and Se along the three principal crystal axes are listed in Table II, and found to be in good agreement with the values determined from structural refinements. As observed, a rapid increase in the ADPs was found above 600 K. The increase is associated with the structural transformation and not related to the already low thermal conductivity. The calculated ADPs are close but larger than the mean square displacements derived from NRIXS measurements at similar temperatures seen in Fig. 2. This is related to the fact that the AIMD calculated DOS have modes at slightly lower energies compared to NRIXS results.

TABLE II. Anisotropic atomic displacement parameters computed from AIMD simulations. All in unit of Å^2.

	Sn				Se			
T (K)	U^{11}	U^{22}	U^{33}	U^{iso}	U^{11}	U^{22}	U^{33}	U^{iso}
200	0.012	0.011	0.013	0.012	0.010	0.009	0.010	0.010
300	0.018	0.016	0.019	0.018	0.015	0.013	0.014	0.014
410	0.041	0.029	0.028	0.033	0.037	0.023	0.023	0.027
600	0.040	0.038	0.046	0.041	0.033	0.028	0.030	0.030
800	0.066	0.051	0.053	0.057	0.040	0.044	0.050	0.045

Phonon DOS was computed from the Fourier transform of the atomic velocity autocorrelation function. The resulting Sn partial phonon DOS are plotted in Fig. 3. The results compare well with NRIXS measurements (Fig. 1) at corresponding temperatures, particularly 200 K and 300 K. The spectral features are correctly reproduced by AIMD calculation. In addition to the polycrystalline average comparison here, the directional phonon DOS can be calculated and show good agreement with those determined experimentally from a single crystal at room temperature [23]. At low temperatures the DOS feature two separated regions of optical modes, at below 10 meV and around 17 meV. At high temperatures, the gap between optical modes of low and high energies is filled. This can be seen in Fig. 1, and was observed also in an inelastic neutron scattering

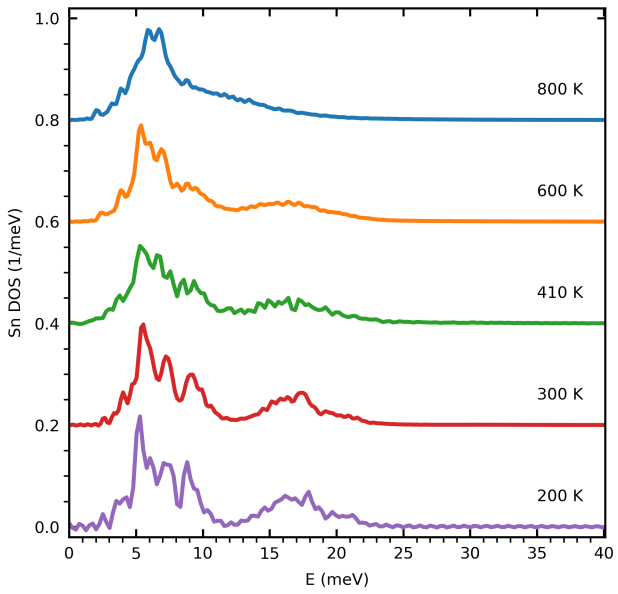

FIG. 3. Sn partial phonon DOS derived from AIMD simulations.

study [10]. AIMD simulation shows the same behaviour from 410 to 800 K.

In Fig. 4, Sn and Se partial DOS from AIMD simulations at 300 K and 600 K are compared to the NRIXS measured Sn partial DOS at 298 K and the phonon dispersions from athermal lattice dynamics (LD) calculations using the same 2x5x5 supercell. At 300 K, the agreement between the calculated and observed Sn partial DOS is remarkable. The Sn and Se DOS computed from MD at 300 K also agree well with the LD results, both on the positions of the peaks and the widths of the distribution. The observation suggests there is little anharmonic effect from 0 to 300 K. This is also supported by the almost flat R_3 moments in Fig. 2. The optical modes are separated by a gap at around 12.5 meV in the LD calculation, and can be seen in MD simulations and NRIXS results as well. Going from 300 to 600 K, changes of the lower optical modes and acoustic modes appear to be minor but subtle. Changes in the upper optical modes are more striking. The zone center optical modes of Sn at 17.5 meV is lowered to 16.0 meV and become much more broad. The optical mode maximum of Se changes from 16.0 to 14.5 meV. The results clearly indicate softening of the optical vibrations for both Sn and Se. Besides, the bandwidth of the upper optical branch has increased substantially, which indicates the shortening of phonon lifetimes of these optical modes. This is particularly true for the Sn optical modes.

SnSe exhibits an extraordinarily low thermal conductivity even at ambient temperature. Several theoretical calculations have been performed to predict and explain the low values [8, 9]. Most studies employ the Boltzmann transport equation (BTE) in the single relaxation time

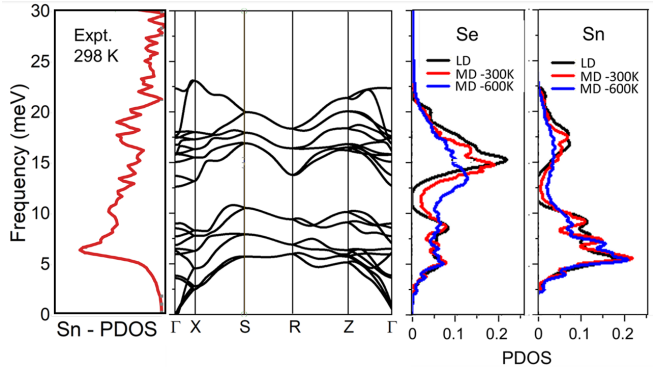

FIG. 4. Comparison of phonon DOS measured using NRIXS and calculated with AIMD to phonon dispersions from athermal LD calculation.

approximation [32] in which the phonon lifetimes were computed from the third order force constants using finite displacement methods employing the harmonic frequencies, group velocities and mode heat capacities obtained from lattice dynamic method. These approaches may not be suitable at high temperatures due to very large anharmonicity and structural transition to the entropically stabilized high temperature *Cmcm* phase. In this case, the force constant based method requires corrections to the third order force constants and the renormalization of the harmonic frequencies as were done in a recent study [9]. As shown above, there are significant changes in the phonon frequencies and lifetimes even in the low temperature *Pnma* phase.

A direct MD based method is more appropriate due to implicit inclusion of the anharmonicity of the interaction potentials and the temperature effect on the dynamics and unit cell expansion. The method has been shown to be accurate for ordered and disordered solids close to and above Debye temperature [13–15]. The thermal conductivity was calculated employing the Einstein diffusion equation [33, 34] without resorting to the computation of the heat flux correlation function as in the common Green-Kubo approach. In this method heat conduction is expressed in an energy moment vector [15],

$$\boldsymbol{R} = \sum_i \epsilon_i \boldsymbol{r}_i \,, \tag{11}$$

where ϵ_i is the energy of the i-th atom. The heat flux vector $\boldsymbol{J}$ is the rate of change of this energy moment, $\boldsymbol{J} = d\boldsymbol{R}/dt$. In a solid, the atoms are not diffusive and the convection contribution is negligible. As a result, the potential portion of $\boldsymbol{R}$ can be ignored and only the kinetic part remains [15],

$$\boldsymbol{R}_k = \sum_i \boldsymbol{r}_i \int \boldsymbol{F}_i \cdot \boldsymbol{v}_i \, dt \,. \tag{12}$$

This expression has been shown to be valid for N-body potentials. The instantaneous position $\boldsymbol{r}_i$, velocity $\boldsymbol{v}_i$ and $\boldsymbol{F}_i$ are readily available in an *ab initio* MD calculation.

Instead of computing from the integration of the heat flux autocorrelation, the thermal conductivity κ can be computed using an equivalent Einstein relationship from the mean square difference (MSD) of the energy moment diffusion,

$$\kappa = \frac{1}{V k_B T^2} \lim_{t\to\infty} \frac{1}{2t} \langle [\boldsymbol{R}(t) - \boldsymbol{R}(0)]^2 \rangle \,, \tag{13}$$

where V is the volume and k_B is the Boltzmann constant. The procedure is illustrated in Fig. 5 for the simulation on the thermal conductivity SnSe at 300K. Typically, a MD trajectory over 0.60 ns is needed.

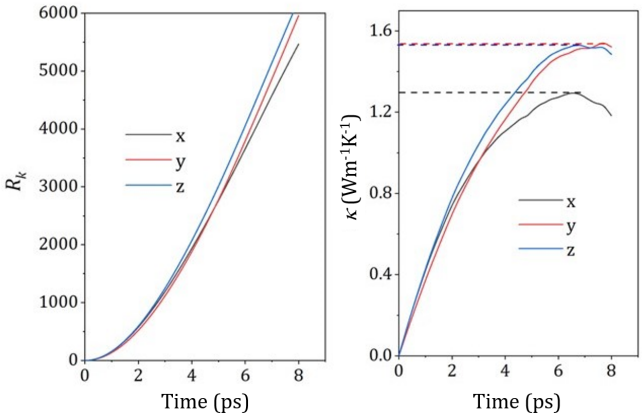

FIG. 5. The x, y and z components of energy momenta $\boldsymbol{R}_k$ are found to propagate with increasing time (left) . The slopes of the MSD of $\boldsymbol{R}_k$ (Eq.(13)) give the thermal conductivity along the three directions. The corresponding thermal conductivities as a function of time are shown on the right. In each case, the function reaches a steady state appears as a plateau which gives the limiting thermal conductivity. The statistical errors were estimated from the averages over multiple time origins by subdividing equal segments of the long MD trajectory.

Results of the calculations on the thermal conductivity along the three principal crystallographic axes of SnSe in the *Pnma* phase below and at 600 K and in the *Cmcm* phase at 800 K are summarized in Table III, where and hereafter in the text all thermal conductivities are reported in the unit of $Wm^{-1}K^{-1}$, which will be omitted to save space.

The temperature dependent thermal conductivities (κ), particularly the observed trend ($\kappa_c \approx \kappa_b > \kappa_a$) above 300 K are reproduced. The order is to be expected as the unit cell lengths $a \gg b \approx c$. The absolute magnitudes are also consistent with previous BTE calculations. Direct comparison to measured values needs to be cautious [35]. The experimental thermal conductivity of SnSe is strongly dependent on the quality of the samples in terms of, *e.g.*, density, purity, crystallinity, stoichiometry, intrinsic and extrinsic defects, *etc.* In the initial report [3], the thermal conductivity along the a-axis, κ_a, decreased from 0.46 at 300 K to 0.25 at 600 K,

TABLE III. Thermal conductivities along the three principal crystallographic axes of SnSe in the *Pnma* and *Cmcm* phases computed from AIMD simulations. All in the unit of $Wm^{-1}K^{-1}$. The errors were estimated from analysis of the results calculated from several segments of the trajectory with different lengths and at different time origins.

T(K)	κ_a	κ_b	κ_c
200	1.38 ± 0.29	2.33 ± 0.34	1.92 ± 0.31
300	1.27 ± 0.18	1.51 ± 0.23	1.53 ± 0.24
410	0.98 ± 0.15	1.18 ± 0.18	1.15 ± 0.21
600	0.56 ± 0.08	0.74 ± 0.10	0.76 ± 0.11
800	0.45 ± 0.05	0.57 ± 0.07	0.56 ± 0.08

and remained fairly constant and low at higher temperatures. A re-evaluation of the literature values [36] suggests that the earlier reported values are likely underestimated. The appropriate values close to pure crystalline SnSe at 300 K should be about 0.7, 0.9 W/m/K in the parallel and 1.1 1.2 W/m/K in the perpendicular direction, and at 750K, 0.3 0.5 W/m/K in the parallel and 0.5 0.7 W/m/K perpendicular direction. The thermal conductivities at 300 K from the single-crystal measurements of Ibrahim [37] are 1.2, 2.3 and 1.7 W/m/K in the a, b and c directions. The thermal conductivity decreases with rising temperature and becomes almost identical to about 1 W/m/K at 750 K. On the other hand, a recent study at 300 K [38] has found a different trend where $\kappa_c(1.5) > \kappa_b(0.8) > \kappa_a(0.5)$. It is noteworthy that at 200 K a large difference between κ_c and κ_b is calculated with the predicted sequence $\kappa_b > \kappa_c > \kappa_a$ agreeing with the low temperature data of Ref. [38]. This can be attributed to the significant difference between the lattice parameters b and c at low temperatures (*vide supra*). With the estimated statistical errors, the theoretical predicted thermal conductivities are within the range of several studies. The exact cause for the discrepancies among the experimental results is difficult to assess. It is likely due to the differences in quality, purity, and stoichiometry of the samples.

The MD method has a distinct advantage over the BTE with LD on layered materials. In the latter method, a spherical cutoff radius has to be defined to include the calculations of third-order interactions on an atom. A spherical cutoff is not efficient for layered structures as the interlayer separation can be much larger than the nearest neighbour distances in the plane. A balanced description of the interactions on an atom may require a very large cutoff radius, hence, involve the laborious enumeration of a very large number of third-order force constants.

An important result which seems to have been overlooked in previous studies is that the computed thermal conductivities show no discernible discontinuity at 800 K and remain fairly constant above 600 K even though there are changes in the lattice stability and significant increase in the anharmonic atomic motions that require renormalization of the phonon frequencies and corrections to the third-order force constants to properly reproduce the observed thermal conductivities. This indicates that intrinsic anharmonic potential responsible for the low thermal conductivity in SnSe is already presented at low temperature, as revealed from the analysis of the NRIXS phonon spectra.

In this paper, new experimental results were presented on the temperature dependence of phonon DOS from ^{119}Sn NRIXS measurements. Analysis of moments of NRIXS spectra indicates that Sn atomic motions deviate from harmonic approximation and become highly anharmonic at around 300 K affecting predominantly optical vibrations. This conclusion agrees with an earlier report on a large temperature effect on the average Grüneisen parameter [38]. It has also been shown that the positions of Sn and Se atoms start to deviate from the low temperature trend at 425 K [30].

AIMD calculations provide additional insight. Directional thermal conductivities of a SnSe crystal were calculated using a recently developed MD method. The results are in substantial agreement with previous experiments highlighting the usefulness of this new approach to study heat transport in highly anisotropic solids.

Observed and calculated Sn partial phonon DOS reveal significant changes in the frequencies and linewidths of the optical phonon modes. This provides evidence that attributes the low thermal conductivity to phonon scattering in the optical branch. The substantial phonon frequency renormalization due to lattice instability accompanying the phase transition has only a minor effect. What changes significantly near the structural transition is the electrical conductivity. Therefore, the sudden surge in the power factor and the performance index ZT is mainly of electronic origin.

I. ACKNOWLEDGMENTS

We thank beamline scientists at APS, Bogdan Leu, Ayman Said, Ahmet Alatas, and E. Ercan Alp, for help with instruments and experiments. This research used resources of the Advanced Photon Source, a U.S. Department of Energy (DOE) Office of Science User Facility operated for the DOE Office of Science by Argonne National Laboratory under Contract No. DE-AC02-06CH11357. We also gratefully acknowledge the computing resources provided on Bebop, a high-performance computing cluster operated by the Laboratory Computing Resource Center at Argonne National Laboratory, and an allocation of computing resources from ComputeCanada.

[1] Z. Nabi, A. Kellou, S. Mabih, A. Khalfi, and N. Benosman, Materials Science and Engineering: B **98**, 104 (2003).

[2] S. S. Siddiqui and C. F. Desai, Crystal Research and Technology **29**, K26 (1994), https://onlinelibrary.wiley.com/doi/pdf/10.1002/crat.2170290225.

[3] L.-D. Zhao, S.-H. Lo, Y. Zhang, H. Sun, G. Tan, C. Uher, C. Wolverton, V. P. Dravid, and M. G. Kanatzidis, Nature **508**, 373 (2014).

[4] W. Shi, M. Gao, J. Wei, J. Gao, C. Fan, E. Ashalley, H. Li, and Z. Wang, Advanced Science **5**, 1700602 (2018), https://onlinelibrary.wiley.com/doi/pdf/10.1002/advs.201700602.

[5] H. G. von Schnering and H. Wiedemeier, Zeitschrift fr Kristallographie - Crystalline Materials **156**, 143 (01 Jan. 1981).

[6] T. Chattopadhyay, J. Pannetier, and H. G. Von Schnering, Journal of Physics and Chemistry of Solids **47**, 879 (1986).

[7] M. Sist, J. Zhang, and B. Brummerstedt Iversen, Acta Crystallographica Section B **72**, 310 (2016).

[8] J. M. Skelton, L. A. Burton, S. C. Parker, A. Walsh, C.-E. Kim, A. Soon, J. Buckeridge, A. A. Sokol, C. R. A. Catlow, A. Togo, and I. Tanaka, Phys. Rev. Lett. **117**, 075502 (2016).

[9] U. Aseginolaza, R. Bianco, L. Monacelli, L. Paulatto, M. Calandra, F. Mauri, A. Bergara, and I. Errea, Phys. Rev. Lett. **122**, 075901 (2019).

[10] C. W. Li, J. Hong, A. F. May, D. Bansal, S. Chi, T. Hong, G. Ehlers, and O. Delaire, Nature Physics **11**, 1063 (2015).

[11] M. Y. Hu, T. S. Toellner, N. Dauphas, E. E. Alp, and J. Zhao, Phys. Rev. B **87**, 064301 (2013).

[12] J. S. Tse, Annual Review of Physical Chemistry **53**, 249 (2002), pMID: 11972009, https://doi.org/10.1146/annurev.physchem.53.090401.105737.

[13] N. J. English and J. S. Tse, Computational Materials Science **126**, 1 (2017).

[14] J. S. Tse, N. J. English, K. Yin, and T. Iitaka, The Journal of Physical Chemistry C **122**, 10682 (2018), https://doi.org/10.1021/acs.jpcc.8b00880.

[15] A. Kinaci, J. B. Haskins, and T. an, The Journal of Chemical Physics **137**, 014106 (2012), https://doi.org/10.1063/1.4731450.

[16] E. Alp, W. Sturhahn, T. Toellner, J. Zhao, M. Hu, and D. Brown, Hyperfine Interactions **144-145**, 3 (2002).

[17] W. Sturhahn, T. S. Toellner, E. E. Alp, X. Zhang, M. Ando, Y. Yoda, S. Kikuta, M. Seto, C. W. Kimball, and B. Dabrowski, Phys. Rev. Lett. **74**, 3832 (1995).

[18] M. Y. Hu, Hyperfine Interactions **237**, 64 (2016).

[19] W. M. Visscher, Annals of Phys. **9**, 194 (1960).

[20] K. S. Singwi and A. Sjölander, Phys. Rev. **120**, 1093 (1960).

[21] W. Sturhahn and V. Kohn, Hyperfine Interactions **123-124**, 367 (1999).

[22] H. J. Lipkin, Phys. Rev. B **52**, 10073 (1995).

[23] D. Bansal, J. Hong, C. W. Li, A. F. May, W. Porter, M. Y. Hu, D. L. Abernathy, and O. Delaire, Phys. Rev. B **94**, 054307 (2016).

[24] T. S. Toellner, A. Alatas, and A. H. Said, Journal of Synchrotron Radiation **18**, 605 (2011).

[25] N. Dauphas, M. Y. Hu, E. M. Baker, J. Hu, F. L. H. Tissot, E. E. Alp, M. Roskosz, J. Zhao, W. Bi, J. Liu, J.-F. Lin, N. X. Nie, and A. Heard, Journal of Synchrotron Radiation **25**, 1581 (2018).

[26] W. Sturhahn, Hyperfine Interactions **125**, 149 (2000).

[27] G. Kresse and J. Furthmüller, Phys. Rev. B **54**, 11169 (1996).

[28] G. Kresse and D. Joubert, Phys. Rev. B **59**, 1758 (1999).

[29] M. P. Allen and D. J. Tildesley, *Computer simulation of liquids*, 2nd ed. (Oxford University Press, 2017).

[30] I. Loa, S. R. Popuri, A. D. Fortes, and J. W. G. Bos, Phys. Rev. Materials **2**, 085405 (2018).

[31] P.-C. Wei, S. Bhattacharya, Y.-F. Liu, F. Liu, J. He, Y.-H. Tung, C.-C. Yang, C.-R. Hsing, D.-L. Nguyen, C.-M. Wei, M.-Y. Chou, Y.-C. Lai, T.-L. Hung, S.-Y. Guan, C.-S. Chang, H.-J. Wu, C.-H. Lee, W.-H. Li, R. P. Hermann, Y.-Y. Chen, and A. M. Rao, ACS Omega **4**, 5442 (2019), https://doi.org/10.1021/acsomega.8b03323.

[32] W. Li, J. Carrete, N. A. Katcho, and N. Mingo, Computer Physics Communications **185**, 1747 (2014).

[33] D. A. McQuarrie, *Statistical Mechanics* (Harper & Row Publishers, 1976).

[34] E. Helfand, Phys. Rev. **119**, 1 (1960).

[35] P.-C. Wei, S. Bhattacharya, J. He, S. Neeleshwar, R. Podila, Y. Y. Chen, and A. M. Rao, Nature **539**, E1 (2016).

[36] L.-D. Zhao, C. Chang, G. Tan, and M. G. Kanatzidis, Energy Environ. Sci. **9**, 3044 (2016).

[37] D. Ibrahim, J.-B. Vaney, S. Sassi, C. Candolfi, V. Ohorodniichuk, P. Levinsky, C. Semprimoschnig, A. Dauscher, and B. Lenoir, Applied Physics Letters **110**, 032103 (2017), https://doi.org/10.1063/1.4974348.

[38] J. S. Kang, H. Wu, M. Li, and Y. Hu, Nano Letters **19**, 4941 (2019), https://doi.org/10.1021/acs.nanolett.9b01056.